Title: Growth Kinetics of Single Polymer Particles in Solution via Active-Feedback 3D Tracking

Authors:

Donggeng Yu[1], Antonio Garcia IV[2], Suzanne A. Blum[2]*, and Kevin D. Welsher[1]*

Affiliations:

[1]Department of Chemistry, Duke University; Durham, NC, 27708, USA

[2]Department of Chemistry, University of California, Irvine; Irvine, CA, 92697, USA

*Corresponding authors. Email: kdw32@duke.edu (K.D.W.); blums@uci.edu (S.A.B.)

Abstract:

The ability to directly observe chemical reactions at the single-molecule and single-particle level has enabled the discovery of behaviors otherwise obscured by the ensemble averaging in bulk measurements.[1-19] However powerful, a common restriction of these studies to date has been the absolute requirement to surface tether or otherwise immobilize the chemical reagent/reaction of interest. This constraint arose from a fundamental limitation of conventional microscopy techniques, which could not track molecules or particles rapidly diffusing in three dimensions, as occurs in solution. However, much chemistry occurs in the solution phase, leaving single-particle/-molecule analysis of this critical area of science beyond the scope of available technology. Here we report the first solution-phase studies and measurements of any chemical reaction at single-particle/-molecule level in freely diffusing solution. During chemical reaction, freely diffusing polymer

particles ($D \sim 10^{-12}$ m^2/s) yielded single-particle 3D trajectories and real-time volumetric images that were analyzed to extract the growth rates of individual particles. These volumetric images show that the average growth rate is a poor representation of the true underlying variability in polymer-particle growth behavior. These data revealed statistically significant populations of faster- and slower-growing particles at different depths in the sample, showing emergent heterogeneity while particles are still in the solution phase. These results go against the prevailing premise that chemical processes freely diffusing in solution will exhibit uniform kinetics. These new understandings of mechanisms behind polymer growth variations bring about an exciting opportunity to control particle-size and plausibly molecular weight polydispersity by the rational design of conditions to dictate spatial growth gradients. We anticipate that these studies will launch a new field of solution-phase, nonensemble-averaged measurements of chemical reactions.

Solution-phase polymerization is vital for modern materials production. These diverse production processes include ring-opening metathesis polymerization (ROMP)[20-22], homogeneous Ziegler–Natta polymerization[23-25], and atom-transfer radical polymerization[26,27]. Traditional analytical techniques used to study polymerization in solution, such as NMR spectroscopy[28,29], fluorescence correlation spectroscopy[30-32], and dynamic light scattering[33-35], provide ensemble averaged information on polymer growth rates, catalyst turnover efficiency, diffusion behavior, and conformational dynamics. These traditional measurement techniques, however, are incapable of measuring polymer behavior at the single-molecule and -particle level. In contrast, at the other end of the analytical regime, single-molecule/particle techniques can provide information on tethered or otherwise restricted polymer behaviors in real-time with high spatial resolution,[17,19,36-40] but to date cannot measure behavior in freely diffusing solution, leaving the solution behavior

of growing polymers at the single-particle level fully unknown. Therefore, an analytical tradeoff has existed up to this point: measure in freely diffusing solution and only acquire ensemble data, *or* measure restricted-diffusion species and reveal single-particle/molecule data. This gap limits the mechanistic understanding of how dynamics in solution impact particle growth, restricting the ability to control and improve these vital catalytic polymerization processes. This analytical tradeoff has existed to date for measuring all chemical reaction processes—beyond simply the polymerization reaction described here.

Ruthenium catalyzed ROMP of norbornene and its derivatives are synthetically and industrially important processes[41] where immobilized single-molecule and -particle studies previously revealed otherwise hidden heterogeneity. Heterogeneous growth kinetics were observed between individual polymer aggregate particles precipitated onto glass.[11,19] In another study, magnetic tweezers were used to elongate immobilized polymer chains, revealing non-uniform wait-and-jump steps attributed to sudden conformational unfolding during polymer growth.[17] Despite these advances, it remains intriguingly unknown if the growth kinetics of polymers in solution exhibit similar variations in behavior as do these immobilized polymers. Fast dynamics of solvated polymer strands in solution, for example, could lead to a time averaging of the local environments from the perspective of each particle in solution, resulting in uniform growth (Fig. 1a). Similarly, the variation in growth as previously characterized could have been caused by or inherent to the immobilization processes or measurement methods themselves (i.e., the glass surface or the applied force) and thus not be present in solution.[42] Indeed, these molecular ruthenium polymerization catalysts are referred to as "well-defined" due to their set ligand coordination spheres and uniform solution polymerization kinetics when measured by ensemble-averaged analytical techniques.[43,44] However, the degree to which growth is truly uniform in

solution remains unknown, potentially obscured by ensemble averaging, as are mechanisms that give rise to variance (Fig. 1a). The potential variations in—and concurrent mechanisms behind—growth of polymers in solution are of great interest towards the production of monodispersed polymers, including of aggregates.[45]

In a solution-phase chemical reaction, the reactants, products, and catalysts exhibit high-speed diffusion and quickly travel long ranges in three dimensions. Therefore, an extremely sensitive and rapidly responding method is needed to capture chemical reactions in real time at these high speeds with minimal perturbation, as they occur in synthetically relevant conditions. We recently reported 3D single-molecule active real-time tracking (3D-SMART) [46,47] to study single fluorophores and viruses in biological systems. In contrast to biological systems, active chemical reaction systems (such as the polymer example cited above) present a higher challenge for active-feedback tracking for three reasons: 1) Single-particle compositions change during the measurement due to reaction progress, 2) Diffusive speeds of particles are up to 2-to-3-fold faster in low viscosity organic solvents (e.g., toluene, tetrahydrofuran, chloroform, low molecular weight hydrocarbons, and other common solvents for synthetic organic reaction systems) when compared to water,[48,49] and 3) Photon-efficient localization and tracking are critical to minimize photobleaching so as to extend observation time as required for the timescales of most synthetic chemical processes. For these reasons, there has yet to be the demonstration of active-feedback tracking for any solution-phase chemical reaction. To overcome these challenges, we now develop a method to measure the chemical and physical growth dynamics of single-polymer particles in real-time by recording and analyzing their changing volumetric images as they grow during a chemical reaction via 3D-SMART active-feedback tracking.

First, real-time estimates of the polymer particle's position were obtained by scanning a focused laser spot over a small, predefined 3D pattern (1 μm x 1 μm x 2 μm XYZ) around the detection area using a 2D electro-optic deflector (EOD) and tunable acoustic gradient (TAG) lens[50] (scan rates = 50 kHz XY, 70 kHz Z). Real-time feedback was then applied using a piezoelectric stage to "lock on" to the particle and move the sample and counteract the tracked polymer particle's motion. In effect, the sample is moved to hold the freely diffusing polymer particle fixed within the focal volume of the microscope objective without applying any force or perturbation to the growing particle. This active feedback allows continuous, high-speed observation without surface tethering and without the need to physically trap the particle (Fig. 1c, Extended Data Fig. 1).

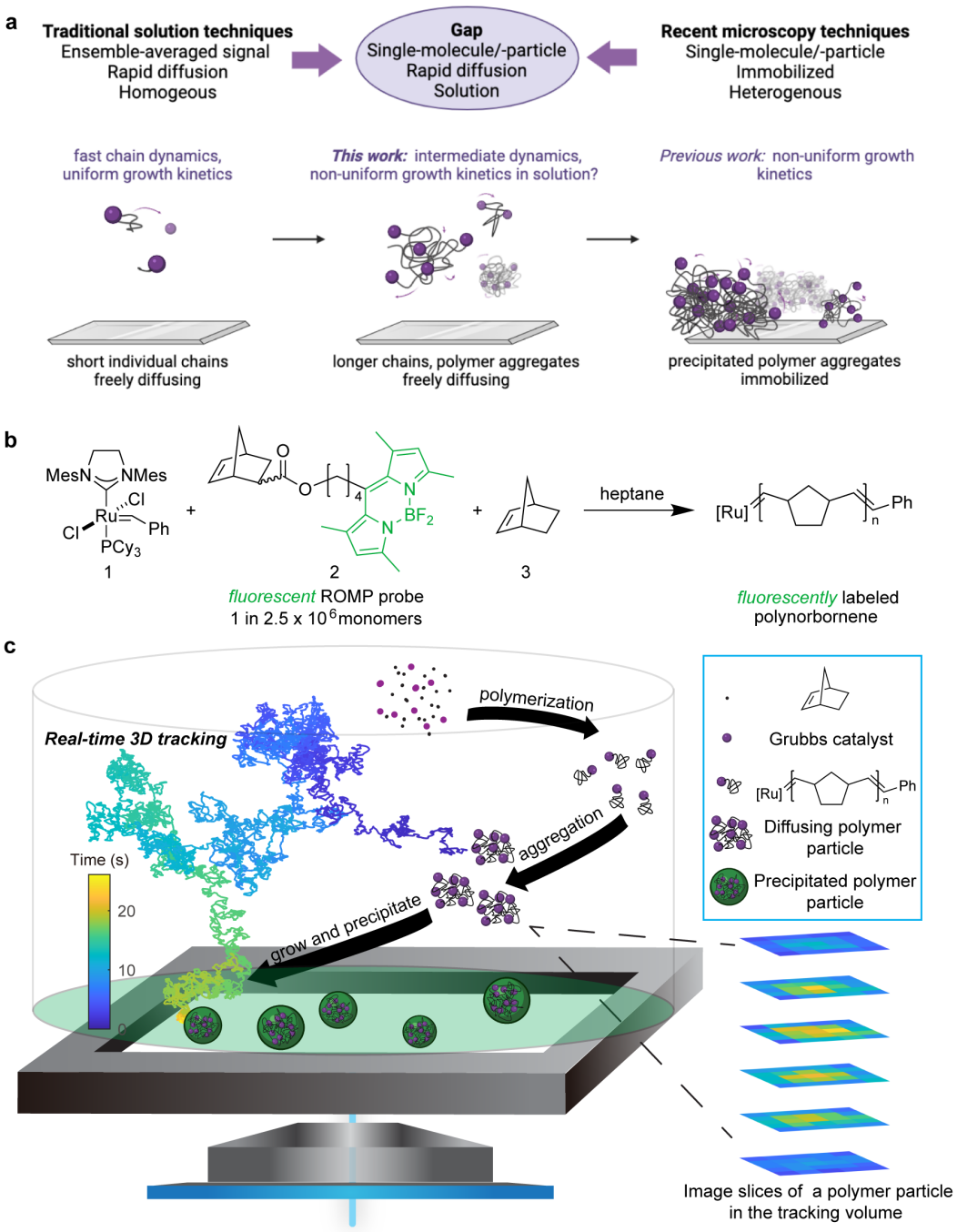

Fig. 1 | Active-feedback tracking of single polymer particle growth. a, Illustration of scientific question and gap in analytical techniques. **b**, Ruthenium-catalyzed ring-opening metathesis polymerization of norbornene (doped with fluorescently labeled norbornene). **c**, Schematic of 3D-SMART. A single polynorbornene particle is captured by and centered within the 3D laser scanning

volume with real-time feedback. The fluorescence emission of the particle is recorded for further analysis.

The ROMP reaction of norbornene (**3**) catalyzed by ruthenium complex **1** (Grubbs 2nd generation catalyst) was initiated in heptane (Fig. 1b).[19] Catalyst, norbornene (5 mM), and boron dipyrromethene (BODIPY) label (**2**) (2 nM) were added in the ratio $1:50:2\times10^{-6}$. The low doping of the fluorescent label and high concentrations of total monomer (mostly unlabeled norbornene) enabled access to synthetically relevant conditions while maintaining the sensitivity needed for single-particle tracking (See Extended Data Fig. 10). When a fluorescently labeled polymer particle (an aggregate containing many polymer strands and catalysts) diffused into the laser scan area, there was a burst in the measured intensity, triggering the start of the feedback loop with the piezoelectric stage. Fig. 2a, b shows a trajectory of a polynorbornene particle that diffused for ~12.5 s and eventually landed on the coverslip. The fluorescence intensity was primarily stable with a slow decrease (attributed to photobleaching) after being calibrated to account for different collection efficiency at varying depths within the sample (Fig. 2c, Extended Data Fig. 3). Analysis of 51 trajectories ($D = (1.3 \pm 0.1) \times 10^{-12}$ m^2s^{-1}) showed that the polynorbornene particles tended to diffuse and descend in the solution and eventually land on the coverslip. These observations were important for two reasons: First, they confirmed the central premise that 3D-SMART could track polymer particles as they diffused in organic solvent in the solution phase. Second, they demonstrated that these particles eventually *became* precipitated particles, similar to those observed to exhibit individualistic growth kinetics in prior immobilized experiments,[19] but now captured here at an earlier stage in the reaction.

A simple way of estimating a diffusing particle's radial size is by calculating the mean

squared displacement (MSD) and applying the Stokes-Einstein relation.[49] However, several challenges are associated with using MSD as a readout of a single polynorbornene particle's size and growth rate. Diffusion is a stochastic process, and even in the absence of any measurement noise, there is a significant variance associated with the extraction of an accurate particle radius from a diffusion coefficient.[51,52] This intrinsic variance, plus the measurement noise associated with 3D localization, led to a sizable uncertainty where no statistically significant changes in the polynorbornene particle size could be extracted (Extended Data Fig. 4). An alternative approach would be to use the increase in fluorescence intensity as more fluorescent monomers are incorporated into the particle. However, the bleaching of BODIPY was non-negligible in these experiments and caused a gradual decrease in fluorescence intensity with time, making intensity an unreliable readout of polynorbornene growth (Fig. 2c).

To overcome these challenges, we developed and implemented an alternative method for estimating the changing size of actively diffusing particles. For real-time feedback, the particle is constantly scanned over a 3D volume. Here we take advantage of this 3D scan and use the photon data acquired at each different laser spot to construct a full volumetric image of the tracked particle as it diffused (Fig. 2d). This 3D image generated from the laser scan of the moving particle was integrated along the axial direction to generate a 2D image. The projected image was fit to a 2D Gaussian distribution (Extended Data Fig. 5), the standard deviation (σ) of which was used as an estimate of the particle radius. Control experiments and calibrations were first run on uniform fluorescent microspheres of known size to correct for the particle radius as a function of depth within the sample (Extended Data Fig. 8). After this calibration, uniform fluorescent microspheres with a manufacturer-specified radius of 478 nm were tracked and exhibited a measured size of 494 ± 4 nm and an average radial growth rate of 0.01 ± 0.01 nm/s, indicating no observable growth

(Fig. 3d). Control experiments on larger microspheres (785 nm) similarly yielded accurate size and no observable growth (770 ± 7 nm; 0.03 ± 0.07 nm/s). These results suggested that the analysis method above successfully estimates the size and the growth rate of freely diffusing fluorescent particles.

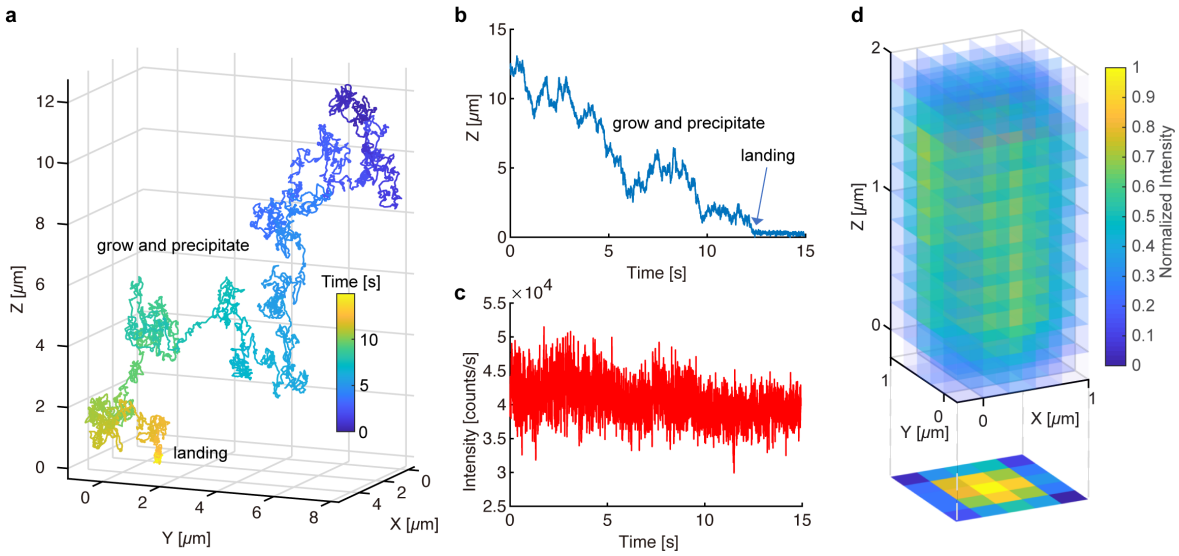

Fig. 2 | 3D trajectory of a growing and freely diffusing polynorbornene particle. a, 3D trajectory of a growing polymer particle that diffuses in heptane. **b**, Z position of the polymer particle as a function of time. The polymer particle lands ~12.5 s. **c**, Fluorescence intensity of the particle as a function of time. **d**, Reconstructed volumetric image of a tracked polymer particle and its integration to the XY-plane.

Applying this technique to polynorbornene particles yielded markedly different results than the uniform microspheres. Most polymer particles exhibited an increasing radius, with a wide range of growth rates (Fig. 3a, b and Extended Data Fig. 8g-i). Radii of tracked particles ranged from 316 – 793 nm, with an average radial growth rate of 0.5 ± 0.1 nm/s (n = 51, Fig. 3c). This growth rate was significantly different ($p < 0.0001$) than that measured for non-growing control

microspheres (0.01 ± 0.01 nm/s). Therefore, it can be concluded that these polymer particles are growing as a function of time as they are tracked in solution.

A remarkable observation from the data above is that the average growth rate was a poor representation of the underlying variability in growth behavior. Although the growth data are best fit by a single normal distribution (Fig. 3c), the single-particle nature of the data allowed us to probe for heterogeneities that correlate with particle parameters. The particle growth rates showed no significant correlation with measured particle size (so number of strands or catalysts as the dominant factor can be ruled out), diffusive speed, or collection time (so "aging" of the solution can be ruled out) (Extended Data Fig. 7).

However, one notable parameter that did show correlation with growth rate was depth within the sample (Fig. 3e, f). A change-point method revealed two populations when split at a distance of 9.3 μm from the surface ($p < 0.01$) (see Methods and Extended Data Fig. 7). The mean growth rate below 9.3 μm was 1.0 ± 0.2 nm/s, and the mean growth rate at 9.3 μm or more above the surface was 0.3 ± 0.1 nm/s. These data indicate that the growth rate heterogeneity arises from spatial heterogeneity within the system. We propose that this spatial heterogeneity is caused by a concentration gradient within the system (Fig 3g): As the reaction progresses, small aggregates form, which precipitate towards the coverslip. Smaller aggregates will be very sparsely labeled (due to the low doping density) and invisible to the tracking system. However, as the larger tracked particle descends, it experiences an ever-higher concentration of these smaller aggregates. This higher concentration leads to an increased growth rate via aggregation as the particle descends. Indeed, the presence of a concentration gradient of small non-tracked aggregates in this system was confirmed via solution-phase fluorescence intensity measurements (see Supplementary Information and Extended Data Fig. 9). Comparison of measured solution radial growth rates with

polymer molecular weights as obtained by GPC (gel permeation chromatography) indicate that the average particle grows by a combination of physical aggregation and chemical monomer insertion (ca. 80:20, see Methods and Supplementary Information), consistent with this proposal. In this proposal, dependent on its position in the sample, each particle grows by a different and time-variable ratio of physical aggregation-to-chemical elongation. Thus, the relative contributions of the two mechanisms leading to radial growth are individualistic to each particle and the average ratio is a poor descriptor of the true behavior.

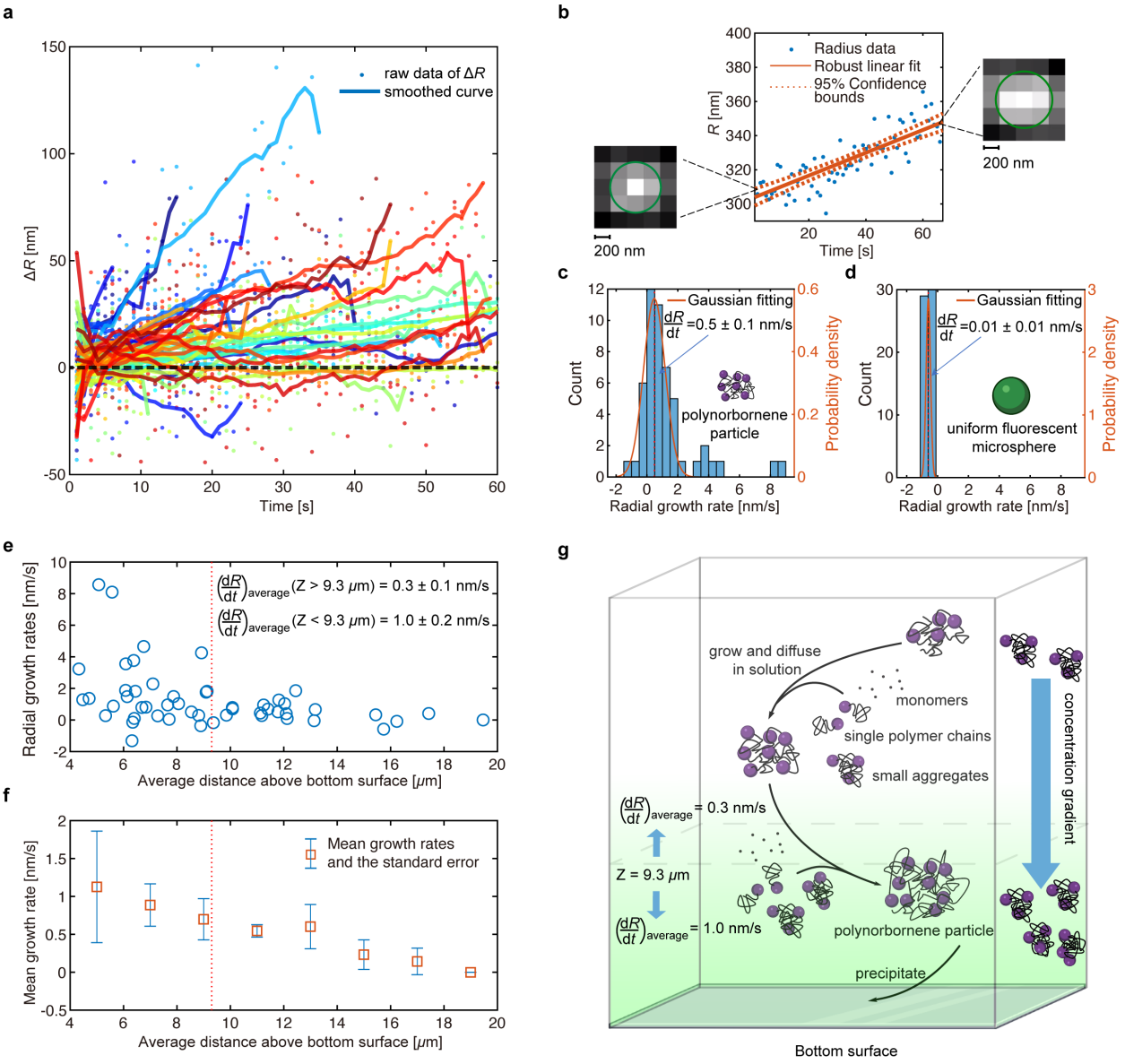

Fig. 3 | Radial growth rates and observed growth heterogeneity from single particles. a, Radius change over time ($\Delta R = R_t - R_0$) of 51 polynorbornene particles as scattered dots and smoothed curve of ΔR. **b**, Representative radius of a polynorbornene particle as a function of time and linear fit of polymer particle growth. 2D images are taken from the beginning and end of the trajectory. Green circle illustrates the radius of the particle fitted from the 2D Gaussian. **c, d** Histogram of the radial growth rates and Gaussian fit of (**c**) polynorbornene particles and (**d**) uniform fluorescent beads. **e**, Radial growth rates of polynorbornene as a function of depth within the sample. **f**, Mean growth rates of the polynorbornene particles as a function of depth within the sample. **g**, Conceptual model of spatial heterogeneity leading to growth rate heterogeneity.

Although polymerization occurred entirely in the solution phase in this study, where uniform growth behavior by well-defined molecular catalysts is reasonably expected,[43,44] individual polymer particles nevertheless exhibited non-uniform, heterogeneous growth kinetics. The suite of conditions for emergence of this non-uniform polymerization behavior (e.g., reaction times, sample depths, particle sizes, catalyst–monomer ratios, reaction solvents) would not be readily predictable from first principles, and are not derivable from ensemble measurements. The impact of such heterogeneous growth at the single-particle level is increased particle size polydispersity, which impacts macroscale polymer properties.[45,53] The characterization of these non-uniform kinetics and the identification of their plausible mechanistic origin may therefore be useful to guide future polymer and catalyst development in the diverse areas of solution-phase polymerization reactions. For example, selection of reaction times, vessel shapes, or initiation rates of catalysts to avoid concentration gradients may provide access to narrower particle-size or molecular weight polydispersity. As a substantial portion of all chemical reactions occur in the solution phase, these studies open realms for fast-tracking studies that generate non-ensemble averaged chemical

insights.

Methods

Instrument and reagents

Extended Data Fig. 1 displays the setup of 3D-SMART. Fig. 1**b** displays the ROMP reaction of norbornene catalyzed by Grubbs catalyst. Catalyst **1** (Grubbs catalyst, 2nd generation) and norbornene **3** were purchased from Sigma–Aldrich and were used as received. Spectrophotometric grade heptane (OmniSolv) was purchased from VWR and used as received. Fluorescently labeled norbornene (Imaging agent **2**) was synthesized using the previously reported procedure[19]. Polystyrene microspheres (dragon green, mean radius: 478 nm) were purchased from Bangs Laboratories, Inc. Fluoresbrite carboxylate Yellow-Green (YG) 1.5-micron microspheres (mean radius: 785 nm) were purchased from Polysciences, Inc.

Construction of reaction cells

Extended Data Fig. 2 displays the reaction cell. Cloning cylinders (10 × 10 mm) were cleaned by sonication in the solution of Alconox detergent power in DI-water for 60 min and rinsed with DI-water six times. To assemble the reaction cell, the cleaned cloning cylinders were attached to the coverslips (25 × 25 mm) by applying epoxy (LOCTITE, setting time is 5 min) outside the cylinders; then, the assembled cells were left to cure overnight or longer and were cleaned by sonication in the solution of Alconox detergent power in DI-water for 60 min and rinsed with DI-water six times. During experiments, the cloning cylinder was covered by another clean coverslip to minimize solvent evaporation.

Preparation of monomer solutions

Fluorescent imaging agent **2** (1.1 mg, 2.4 μmol) was dissolved in 2 mL heptane, resulting in a concentration of 1.2 mM. This solution was diluted by 1000 by taking 1 μL and diluting into 1 mL heptane, giving a final concentration of 1.2 μM. Separately, norbornene **3** (6.0 mg, 64 μmol) was dissolved in 12.5 mL heptane. Then 21 μL of the 1.2 μM imaging agent solution was added to the norbornene solution to give a Final Monomer Solution containing both 5 mM norbornene and 2 nM imaging agent.

Tracking the growing polymer particles

The laser was first focused on the upper surface of the coverslip in the reaction cell and then moved upward for 10 μm to ensure that the laser was focused inside the solution at the beginning of tracking. 0.3 mL of bulk solution was added. 1 mg of 2nd generation Grubbs catalyst **1** was dissolved in 200 μL toluene, and 5 μL of this catalyst solution was added to the Final Monomer Solution to start the polymerization reaction. The final concentrations of the three species are 5 mM norbornene, 2 nM probe **2**, and 100 μM catalyst **1**. The tracking microscope was set ready for capturing any fluorescent particles in the solution.

Gaussian fitting of the real-time image

Photons collected by the APD can be used to reconstruct the 3D image (5×5×11 grids) of the particle being tracked by 3D-SMART (Extended Data Fig. 5). The 3D image was then integrated along the Z-axis to the XY-plane to give the 2D image for the particle size estimate. Finally, a 2D Gaussian distribution was used to fit the image (Extended Data Fig. 5): $f(x,y) = A\exp(-(\frac{(x-x_0)^2}{2\sigma_X^2} + \frac{(y-y_0)^2}{2\sigma_y^2}))$, where A is the amplitude, x_0, y_0 is the center and σ_X, σ_Y are the x and

y spread of the distribution. The polymer aggregates were assumed to be spheres, which makes $\sigma_X = \sigma_Y$. Thus, the function used for fitting would be: $f(x,y) = A\exp(-\frac{(x-x_0)^2+(y-y_0)^2}{2\sigma^2})$, where σ was the parameter for describing the radius R of the polymer aggregates. Photon data are segmented into windows of 1 sec and used to estimate the size of polynorbornene aggregates.

Calibration of radius (R) vs. depth (Z)

It was observed that tracked particles tended to exhibit a larger radius when closer to the surface. To calibrate this apparent change in radius with depth, the uniform fluorescent microspheres with a manufacturer-specified radius of 478 nm (Bangs Laboratories, Inc.) were tracked at different depths within the solution. 59 trajectories of these fluorescent microspheres show that there is still a slight difference of sizes between different microspheres, which is consistent with the manufacture datasheet: for example, for microspheres with a nominal radius of 500 nm, the specification range is from 475 – 525 nm. The scatter plot of the observed radius R vs. the Z positions of these microspheres is shown in Extended Data Fig. 8a (Each color corresponds to a single fluorescent microsphere)**.**

To find the calibration curve for this Z-R effect, we need to focus on microspheres of the same size, which required us to remove some microspheres from the data pool for fitting. Therefore, we applied the following strategy:

1) Calculate the average radius and the average Z positions from each trajectory. Remove data points that have negative average Z positions (indicative of sample motion during acquisition) and the ones with average Z > 25 μm (due to lack of samples collected beyond this depth).

2) Fit the relationship between the average radius (R) and the average depth (Z) to a two-term

exponential.

3) Remove microspheres that deviate from the fitted curve by >3 % from the data pool. This is to remove larger and smaller microspheres for more accurate calibration.

4) Use the refined data points to generate the calibration curve, also described by a two-term exponential.

Extended Data Fig. 6 shows the data processing steps above. With this strategy, the relationship between the depth Z and the observed radius R is given by:$R = (495.5e^{-0.0012\times Z} + 6.991e^{-0.1489\times Z})$, where $R_0 = R(Z = 0) = 502.5$ nm is considered the actual radius of the microsphere observed at the surface of the coverslip. This relationship was then used for the calibration of the polynorbornene particle size. For a particle with an actual size of R_{theo} and an observed radius R_{exp} at a depth of Z, these two numbers should follow the equation below:$R_{exp}/R_{theo} = (495.5e^{-0.0012\times Z} + 6.991e^{-0.1489\times Z})/R_0$

It is noticeable that the fluctuation of radius estimated this way is much less than that in the MSD analysis, which makes the results more convincing. The growth rate was calculated using the linear model for radius and time. The average growth rate of 51 polynorbornene aggregates was 0.5 ± 0.1 nm/s. The same analysis on the fluorescent beads (R = 478 nm) with uniform size gave a growth rate of -0.01 ± 0.01 nm/s, suggesting that the growth rate observed for the polymer aggregates is significant enough to describe the actual growth.

Radial growth rate vs. average depth (Z), diffusion coefficient (D), reaction time (t_r), particle size (R_0) and trajectory length (t_{traj})

Changepoint analysis was used to demonstrate the correlation between growth rates and the

average depth Z. For example, for Z_{split} = 10 μm, average weighted growth rates were calculated for polynorbornene particles that have average Z positions below and above 10 μm, respectively. Here we define the weighted average growth μ_w as below and all growths rate in the later text are referring to the weighted growth rate: $\mu_w = \sum \mu \times weight_{norm}$, $weight = \left|\frac{1}{\mathrm{SE}}\right|$, $weight_{norm} = weight / \sum weight$, where μ is the radial growth rate of particles, SE is the standard error of μ from the robust linear fitting of radius vs. time, and $weight_{norm}$ is the normalized weight of each μ. Adding the weight for calculation aims to reduce the effect of outliers since some of the polynorbornene particles show large growth rates due to large fluctuations in the measured size.

A two-tailed t-test was used to test the null hypothesis that these two populations of growth rates are the same. Results showed that the null hypothesis should be rejected (p = 0.0051) and suggested that these two populations of growth rate are from different distributions. Local minimum p-value was found when Z_{split} = 9.3 μm (p = 0.0028). Z_{split} at large and small distances from the coverslip were not considered to ensure that the number of data points is comparable for the two populations. This changepoint analysis suggests that the polynorbornene particles tend to grow faster when closer to the bottom surface, indicating heterogeneity along the Z direction.

The same analysis was performed to test the correlation between the growth rates and the diffusion coefficient, reaction time, particles size, trajectory length (Extended Data Fig. 7b-e). Results suggested that the diffusion coefficient (D), the reaction time (t_r), and the radius of the polynorbornene particles at the beginning of trajectories (R_0) do not show a significant correlation with the growth rates of polynorbornene particles. However, the trajectory length was observed to be highly correlated to the growth rates. We propose that this effect is due to the previously identified correlation between the average Z position and polymer growth: It takes less time for

the polynorbornene particles closer to the surface to descend and land onto the coverslip. Thus, particles that start at positions close to the surface tend to be tracked for shorter periods of time. To eliminate the possibility of an artifact, we applied the same analysis to the tracking data of commercial fluorescent microspheres of known fixed radius to see if short trajectories intrinsically give faster growth rates. While most fluorescent microspheres were tracked for over 1 minute, we manually cut them into shorter segments ranging from 10 sec to 60 sec and applied changepoint analysis. The results show no apparent difference for the growth rates of microspheres with shorter trajectory lengths and longer trajectory lengths, which supports the previous assumption that short trajectory length does not intrinsically give a higher growth rate and instead that the observations in the polymerization sample correlate with the average particle Z position.

Estimation of the composition of polymer particles

The freely jointed chain model for polymers describes the relationship of the gyration radius R_g and the poly degree n of a polymer chain[54] and for polymers in non-solvent: $R_g = bN^{1/3}$, $N = \frac{nl}{b}$, where b is the Kuhn length or the length of a freely jointed unit for the polymer (1.42 nm for polynorbornene)[17,36], N is the number of freely jointed units, l is the length of a monomer unit (0.62 nm for polynorbornene)[17], and n is the number of monomers in the entire polymer.

In the current work, we assume that each polynorbornene particle can be viewed as an extremely long single chain when estimating the number of monomers since the average chain length measure by the GPC experiments suggests that they are long enough that the head and the tail of each polymer chain are not restricted by each other anymore.

With the observed average radius of polynorbornene aggregates $R_g = 476 \pm 16$ nm and the average

growth rate as 0.5 ± 0.1 nm/s, the number of monomers in one aggregate can be calculated: $n = (R_g/b)^3 \times b \div l = (8.6 \pm 0.9) \times 10^7$, and the observed growth rate: $\left(\frac{dn}{dt}\right)_{observed} = \frac{3R_g^2}{lb^2}\left(\frac{dR_g}{dt}\right) = (2.7 \pm 0.2) \times 10^5$ monomers/s. Based on the GPC experiments (see Supplementary Methods Gel permeation chromatography), the average chain length of polynorbornene in the whole system after 30 min of reaction is 606 ± 67 units, which suggests an average polymerization reaction rate of 0.34 ± 0.04 monomers/s and that the average total number of catalysts in each polynorbornene particle is: $n_{cat} = \frac{n}{606} = (1.4 \pm 0.1) \times 10^5$. So, the theoretical average polymerization reaction rate for each polynorbornene particle is: $\left(\frac{dn}{dt}\right)_{\text{polymerization}} = n_{cat} \times 0.34 = (4.8 \pm 0.7) \times 10^4$ monomers/s. Comparing $\left(\frac{dn}{dt}\right)_{\text{polymerization}}$ to the observed growth rate $\left(\frac{dn}{dt}\right)_{\text{observed}}$, it can be estimated that the polymerization reaction causes 18% of the radial growth, while the remaining 82% results from aggregation.

Data Availability

Trajectories of growing polymer particles collected with the 3D-SMART microscope are available upon request.

Code Availability

MATLAB codes for analyzing particle growth trajectories can be found at:

https://github.com/welsherlab/polymertracking

References and Notes

1 Cordes, T. & Blum, S. A. Opportunities and challenges in single-molecule and single-particle fluorescence microscopy for mechanistic studies of chemical reactions. *Nature Chemistry* **5**, 993-999, doi:10.1038/nchem.1800 (2013).

2 Roeffaers, M. B. *et al.* Spatially resolved observation of crystal-face-dependent catalysis by single turnover counting. *Nature* **439**, 572-575 (2006).
3 Xu, W., Kong, J. S., Yeh, Y.-T. E. & Chen, P. Single-molecule nanocatalysis reveals heterogeneous reaction pathways and catalytic dynamics. *Nature Materials* **7**, 992-996, doi:10.1038/nmat2319 (2008).
4 Tachikawa, T., Fujitsuka, M. & Majima, T. Mechanistic Insight into the TiO2 Photocatalytic Reactions: Design of New Photocatalysts. *J. Phys. Chem. C* **111**, 5259-5275, doi:10.1021/jp069005u (2007).
5 Decan, M. R., Impellizzeri, S., Marin, M. L. & Scaiano, J. C. Copper nanoparticle heterogeneous catalytic 'click' cycloaddition confirmed by single-molecule spectroscopy. *Nature Communications* **5**, 4612, doi:10.1038/ncomms5612 (2014).
6 Shen, M. *et al.* Nanoscale Colocalization of Fluorogenic Probes Reveals the Role of Oxygen Vacancies in the Photocatalytic Activity of Tungsten Oxide Nanowires. *ACS Catalysis* **10**, 2088-2099, doi:10.1021/acscatal.9b04481 (2020).
7 Dong, B., Mansour, N., Huang, T.-X., Huang, W. & Fang, N. Single molecule fluorescence imaging of nanoconfinement in porous materials. *Chemical Society Reviews* **50**, 6483-6506, doi:10.1039/D0CS01568G (2021).
8 Kubarev, A. V., Janssen, K. P. F. & Roeffaers, M. B. J. Noninvasive Nanoscopy Uncovers the Impact of the Hierarchical Porous Structure on the Catalytic Activity of Single Dealuminated Mordenite Crystals. *ChemCatChem* **7**, 3646-3650 (2015).
9 Ristanović, Z. *et al.* High-Resolution Single-Molecule Fluorescence Imaging of Zeolite Aggregates within Real-Life Fluid Catalytic Cracking Particles. *Angewandte Chemie International Edition* **54**, 1836-1840, doi:https://doi.org/10.1002/anie.201410236 (2015).
10 Menges, J. A., Grandjean, A., Clasen, A. & Jung, G. Kinetics of Palladium(0)-Allyl Interactions in the Tsuji-Trost Reaction, derived from Single-Molecule Fluorescence Microscopy. *ChemCatChem* **12**, 2630-2637, doi:https://doi.org/10.1002/cctc.202000032 (2020).
11 Garcia Iv, A. *et al.* Does Selectivity of Molecular Catalysts Change with Time? Polymerization Imaged by Single-Molecule Spectroscopy. *Angewandte Chemie International Edition* **60**, 1550-1555, doi:https://doi.org/10.1002/anie.202010101 (2021).
12 Rybina, A. *et al.* Distinguishing Alternative Reaction Pathways by Single-Molecule Fluorescence Spectroscopy. *Angewandte Chemie International Edition* **52**, 6322-6325, doi:https://doi.org/10.1002/anie.201300100 (2013).
13 Feng, C., Cunningham, D. W., Easter, Q. T. & Blum, S. A. Role of LiCl in Generating Soluble Organozinc Reagents. *Journal of the American Chemical Society* **138**, 11156-11159, doi:10.1021/jacs.6b08465 (2016).
14 Ng, J. D. *et al.* Single-Molecule Investigation of Initiation Dynamics of an Organometallic Catalyst. *Journal of the American Chemical Society* **138**, 3876-3883, doi:10.1021/jacs.6b00357 (2016).
15 Chen, P. *et al.* Spatiotemporal catalytic dynamics within single nanocatalysts revealed by single-molecule microscopy. *Chem Soc Rev* **43**, 1107-1117, doi:10.1039/c3cs60215j (2014).
16 Easter, Q. T. & Blum, S. A. Single Turnover at Molecular Polymerization Catalysts Reveals Spatiotemporally Resolved Reactions. *Angewandte Chemie International Edition* **56**, 13772-13775, doi:10.1002/anie.201708284 (2017).
17 Liu, C. *et al.* Single polymer growth dynamics. *Science* **358**, 352-355, doi:10.1126/science.aan6837 (2017).

18 Easter, Q. T. & Blum, S. A. Kinetics of the Same Reaction Monitored over Nine Orders of Magnitude in Concentration: When Are Unique Subensemble and Single-Turnover Reactivity Displayed? *Angewandte Chemie International Edition* **57**, 12027-12032, doi:https://doi.org/10.1002/anie.201807317 (2018).
19 Easter, Q. T. & Blum, S. A. Evidence for Dynamic Chemical Kinetics at Individual Molecular Ruthenium Catalysts. *Angewandte Chemie International Edition* **57**, 1572-1575, doi:https://doi.org/10.1002/anie.201711314 (2018).
20 Liu, P. & Ai, C. Olefin Metathesis Reaction in Rubber Chemistry and Industry and Beyond. *Industrial & Engineering Chemistry Research* **57**, 3807-3820, doi:10.1021/acs.iecr.7b03830 (2018).
21 Bielawski, C. W. & Grubbs, R. H. Living ring-opening metathesis polymerization. *Progress in Polymer Science* **32**, 1-29, doi:10.1016/j.progpolymsci.2006.08.006 (2007).
22 Sutthasupa, S., Shiotsuki, M. & Sanda, F. Recent advances in ring-opening metathesis polymerization, and application to synthesis of functional materials. *Polymer Journal* **42**, 905-915, doi:10.1038/pj.2010.94 (2010).
23 Delferro, M. & Marks, T. J. Multinuclear Olefin Polymerization Catalysts. *Chemical Reviews* **111**, 2450-2485, doi:10.1021/cr1003634 (2011).
24 Makio, H., Terao, H., Iwashita, A. & Fujita, T. FI Catalysts for Olefin Polymerization—A Comprehensive Treatment. *Chemical Reviews* **111**, 2363-2449, doi:10.1021/cr100294r (2011).
25 Brintzinger, H. H., Fischer, D., Mülhaupt, R., Rieger, B. & Waymouth, R. M. Stereospecific Olefin Polymerization with Chiral Metallocene Catalysts. *Angewandte Chemie International Edition in English* **34**, 1143-1170, doi:10.1002/anie.199511431 (1995).
26 Matyjaszewski, K. Atom Transfer Radical Polymerization (ATRP): Current Status and Future Perspectives. *Macromolecules* **45**, 4015-4039, doi:10.1021/ma3001719 (2012).
27 Matyjaszewski, K. Advanced Materials by Atom Transfer Radical Polymerization. *Advanced Materials* **30**, 1706441, doi:10.1002/adma.201706441 (2018).
28 Chen, A., Wu, D. & Johnson, C. S. Determination of Molecular Weight Distributions for Polymers by Diffusion-Ordered NMR. *Journal of the American Chemical Society* **117**, 7965-7970, doi:10.1021/ja00135a015 (1995).
29 Rubens, M., Van Herck, J. & Junkers, T. Automated Polymer Synthesis Platform for Integrated Conversion Targeting Based on Inline Benchtop NMR. *ACS Macro Letters* **8**, 1437-1441, doi:10.1021/acsmacrolett.9b00767 (2019).
30 Zettl, H. *et al.* Fluorescence Correlation Spectroscopy of Single Dye-Labeled Polymers in Organic Solvents. *Macromolecules* **37**, 1917-1920, doi:10.1021/ma035929t (2004).
31 Wöll, D. Fluorescence correlation spectroscopy in polymer science. *RSC Adv.* **4**, 2447-2465, doi:10.1039/c3ra44909b (2014).
32 Weger, L. *et al.* Polymer Diffusion in the Interphase Between Surface and Solution. *Langmuir* **34**, 7021-7027, doi:10.1021/acs.langmuir.8b00660 (2018).
33 Liverpool, T. B. & Maggs, A. C. Dynamic Scattering from Semiflexible Polymers. *Macromolecules* **34**, 6064-6073, doi:10.1021/ma001468p (2001).
34 Tassieri, M. Dynamics of Semiflexible Polymer Solutions in the Tightly Entangled Concentration Regime. *Macromolecules* **50**, 5611-5618, doi:10.1021/acs.macromol.7b01024 (2017).
35 Wang, Z.-G. 50th Anniversary Perspective: Polymer Conformation—A Pedagogical Review. *Macromolecules* **50**, 9073-9114, doi:10.1021/acs.macromol.7b01518 (2017).

36 Mai, D. J., Saadat, A., Khomami, B. & Schroeder, C. M. Stretching Dynamics of Single Comb Polymers in Extensional Flow. *Macromolecules* **51**, 1507-1517, doi:10.1021/acs.macromol.7b02759 (2018).
37 Li, S. & Schroeder, C. M. Synthesis and Direct Observation of Thermoresponsive DNA Copolymers. *ACS Macro Letters* **7**, 281-286, doi:10.1021/acsmacrolett.8b00016 (2018).
38 Easter, Q. T. & Blum, S. A. Kinetics of the Same Reaction Monitored over Nine Orders of Magnitude in Concentration: When Are Unique Subensemble and Single-Turnover Reactivity Displayed? *Angewandte Chemie International Edition* **57**, 12027-12032, doi:10.1002/anie.201807317 (2018).
39 Easter, Q. T. & Blum, S. A. Single Turnover at Molecular Polymerization Catalysts Reveals Spatiotemporally Resolved Reactions. *Angew Chem Int Ed Engl* **56**, 13772-13775, doi:10.1002/anie.201708284 (2017).
40 Wöll, D. *et al.* Polymers and single molecule fluorescence spectroscopy, what can we learn? *Chem. Soc. Rev.* **38**, 313-328, doi:10.1039/b704319h (2009).
41 Grela, K. *Olefin Metathesis: Theory and Practice*. (John Wiley & Sons, Inc., 2014).
42 Skaug, M. J., Mabry, J. N. & Schwartz, D. K. Single-Molecule Tracking of Polymer Surface Diffusion. *Journal of the American Chemical Society* **136**, 1327-1332, doi:10.1021/ja407396v (2014).
43 Dias, E. L., Nguyen, S. T. & Grubbs, R. H. Well-Defined Ruthenium Olefin Metathesis Catalysts: Mechanism and Activity. *Journal of the American Chemical Society* **119**, 3887-3897, doi:10.1021/ja963136z (1997).
44 Buchmeiser, M. R. Polymer-Supported Well-Defined Metathesis Catalysts. *Chemical Reviews* **109**, 303-321, doi:10.1021/cr800207n (2009).
45 Haehnle, B., Jathavedan, K. K., Schuster, P. A., Karg, M. & Kuehne, A. J. C. Elucidating the Nucleation Event in the C–C Cross-Coupling Step-Growth Dispersion Polymerization. *Macromolecules* **54**, 6085-6089, doi:10.1021/acs.macromol.1c00899 (2021).
46 Hou, S., Exell, J. & Welsher, K. Real-time 3D single molecule tracking. *Nature Communications* **11**, 3607, doi:10.1038/s41467-020-17444-6 (2020).
47 Hou, S., Lang, X. & Welsher, K. Robust real-time 3D single-particle tracking using a dynamically moving laser spot. *Opt. Lett.* **42**, 2390-2393, doi:10.1364/OL.42.002390 (2017).
48 "Viscosity of Liquids" in *CRC Handbook of Chemistry and Physics*, 102nd Edition (Internet Version 2021, John R. Rumble, ed., CRC Press/Taylor & Francis, Boca Raton, Fl.
49 Einstein, A. The motion of elements suspended in static liquids as claimed in the molecular kinetic theory of heat. *Annalen Der Physik* **17**, 549-560 (1905).
50 Mermillod-Blondin, A., McLeod, E. & Arnold, C. B. High-speed varifocal imaging with a tunable acoustic gradient index of refraction lens. *Optics Letters* **33**, 2146-2148, doi:10.1364/OL.33.002146 (2008).
51 Qian, H., Sheetz, M. P. & Elson, E. L. Single particle tracking. Analysis of diffusion and flow in two-dimensional systems. *Biophys J* **60**, 910-921, doi:10.1016/s0006-3495(91)82125-7 (1991).
52 Michalet, X. Mean square displacement analysis of single-particle trajectories with localization error: Brownian motion in an isotropic medium. *Physical Review E* **82**, 041914, doi:10.1103/PhysRevE.82.041914 (2010).
53 Schöpe, H. J., Marnette, O., van Megen, W. & Bryant, G. Preparation and Characterization of Particles with Small Differences in Polydispersity. *Langmuir* **23**, 11534-11539, doi:10.1021/la7018132 (2007).

54 Rubinstein, M. & Colby, R. H. *Polymer physics*. Vol. 23 (Oxford university press New York, 2003).

Acknowledgments:

Funding for this work was provided by the U.S. Department of Energy (DE-SC0016467, to S.A.B.), the American Chemical Society–Petroleum Research Fund (56315-ND4, to S.A.B.), the Allergan Foundation (to A.G.IV), and Duke University (to K.D.W).

Author Contributions:

K.D.W. and S.A.B. conceived of the project idea. A.G.IV synthesized the fluorescently labeled norbornene. D.Y. and A.G.IV performed initial tracking experiment optimizations. D.Y. performed and analyzed GPC experiments and subsequent particle tracking experiments, including statistical analyses. K.D.W., S.A.B., and A.G.IV assisted with analysis of data. S.A.B. and D.Y. prepared the figures. D.Y., K.D.W., S.A.B. and A.G.IV wrote and revised the manuscript and approved the final version.

Competing interests:

The authors declare no competing interests.

Additional information:

Supplementary Information is available for this paper.

Extended data figures and tables

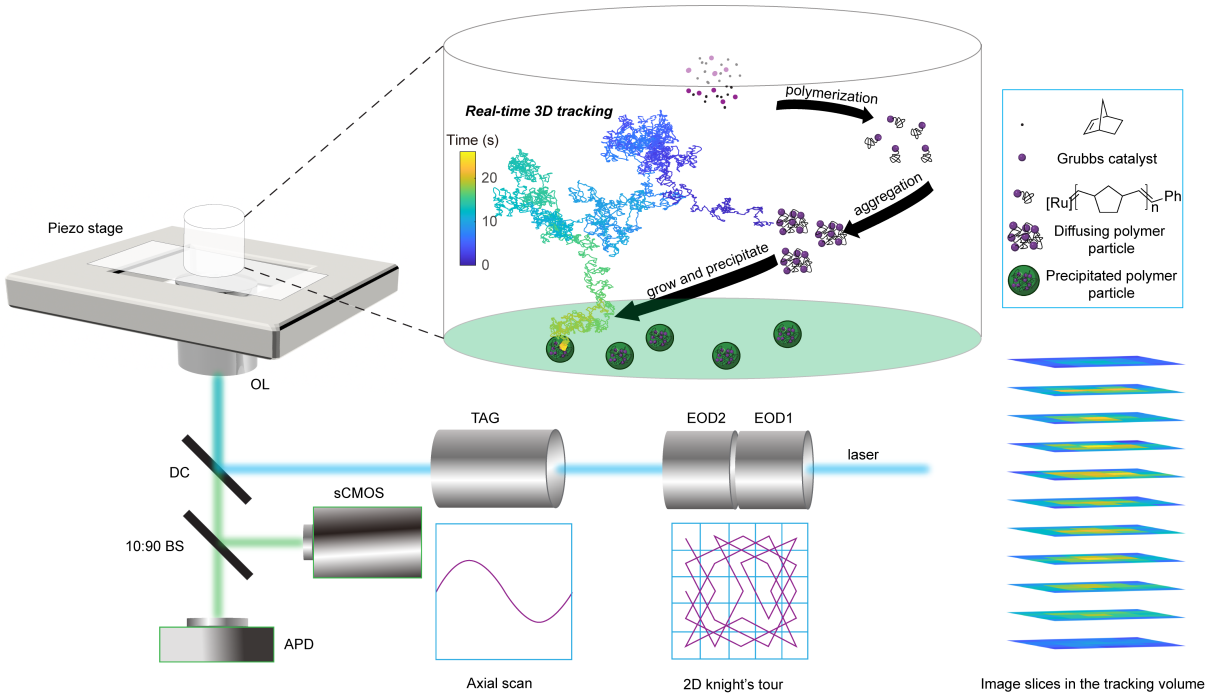

Extended Data Fig. 1 3D-SMART setup. The 2D-EOD (**EOD1** & **EOD2**) and the TAG lens (**TAG**) deflect the laser along the XY-plane over a 5×5 knight's tour pattern and Z directions, respectively. Collected photons are split onto an avalanche photodiode (**APD**, 90%) and a monitor camera (sCMOS,10%). Photon arrival times are used to determine the position of the particle in real-time, which is sent to a 3D piezo stage to counteract the particle's motion and effectively lock it in the focal volume of the objective lens

a

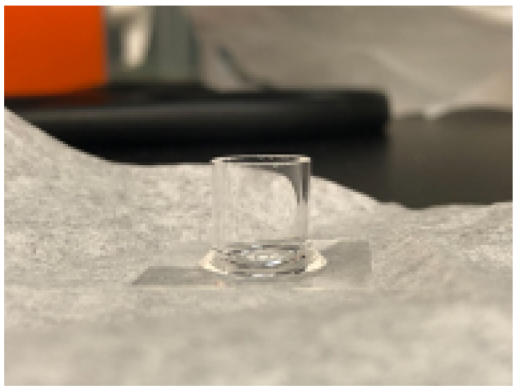

b

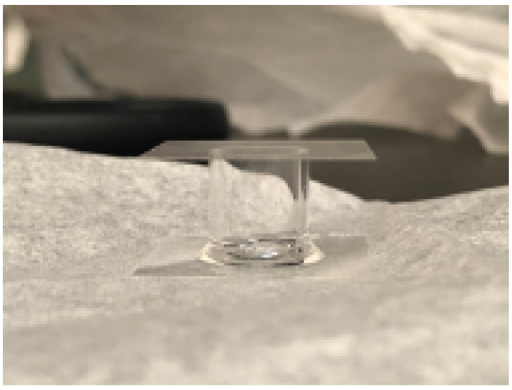

Extended Data Fig. 2 Reaction cell. a, Reaction cell. **b**, Reaction cell covered by a clean coverslip.

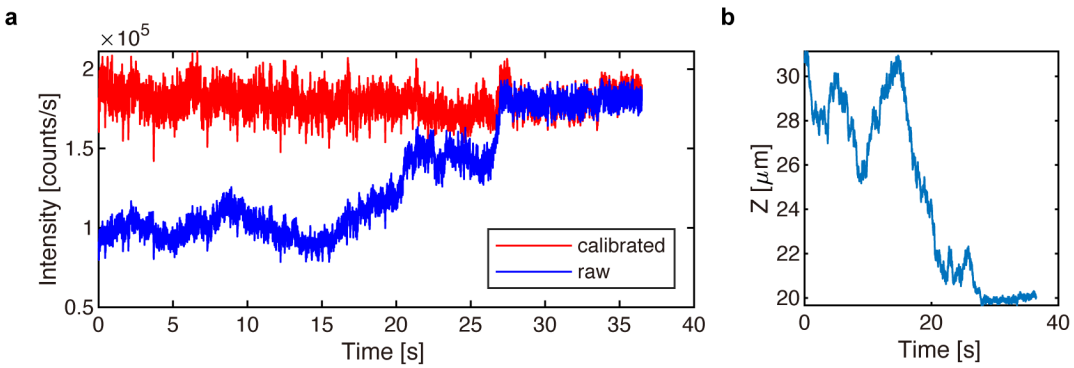

Extended Data Fig. 3 Calibration of fluorescence intensity. a, An example of calibrated intensity (red) vs. detected intensity (blue) as functions of time. **b**, *Z* position of the aggregate as a function of time.

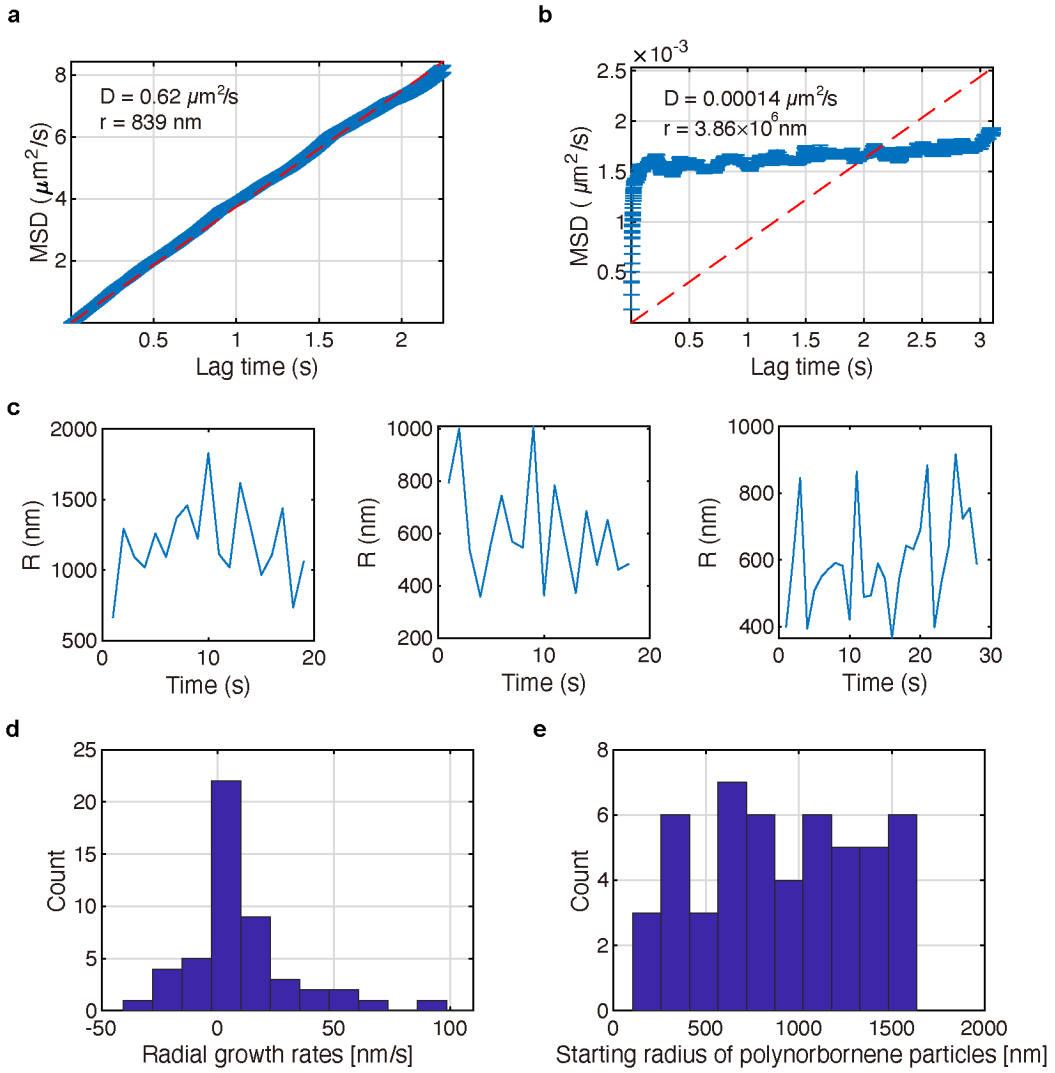

Extended Data Fig. 4 Mean square displacement (*MSD*) analysis. a, MSD as a function of lag time τ when the polymer diffuses in solution. **b**, MSD as a function of lag time τ after the polymer landed on the coverslip. **c**, Three examples of the radius of polynorbornene aggregates calculated from MSD. **d**, Radial growth rates of polynorbornene particles. **e**, Radius of polynorbornene particles at the beginning of each trajectory.

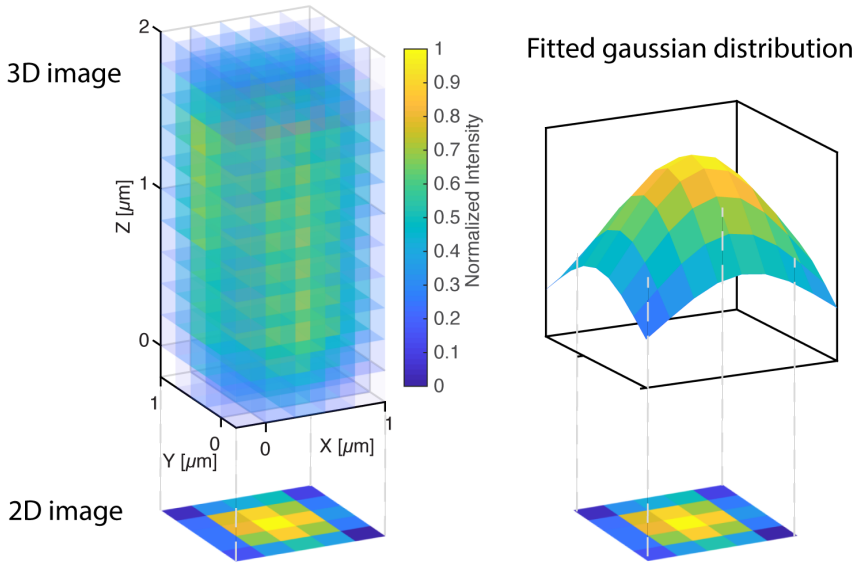

Extended Data Fig. 5 Reconstructed image of a polymer aggregate and the fitted 2D Gaussian distribution (shown in a larger area than the 2D image for a clearer illustration).

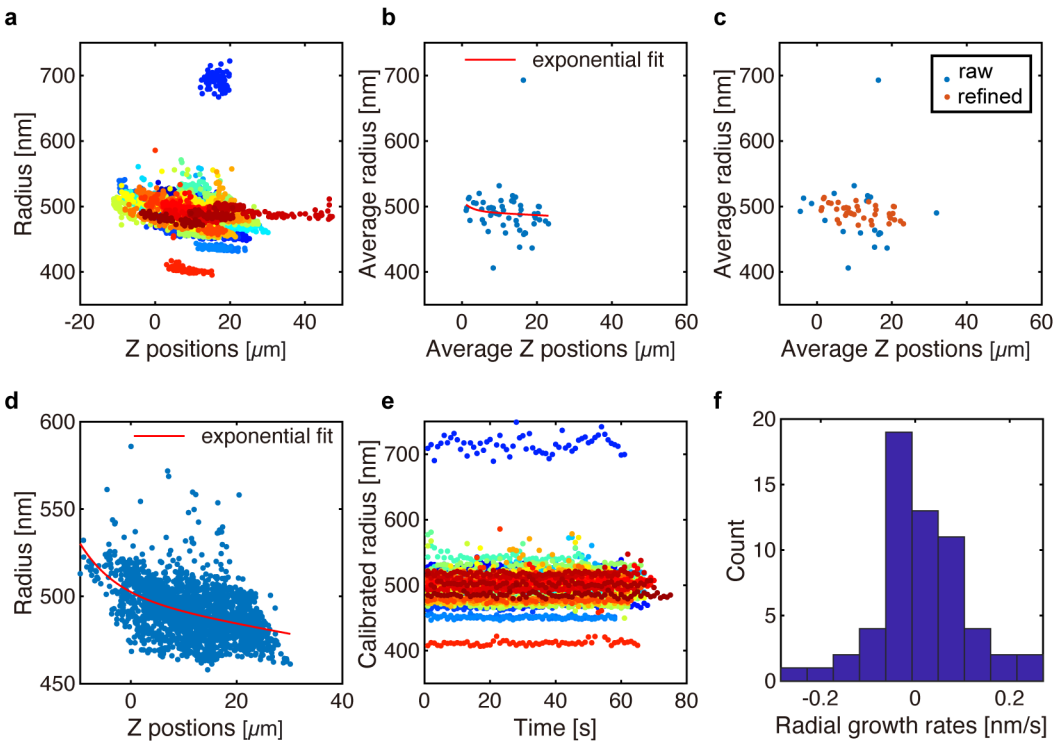

Extended Data Fig. 6 Calibration of radius vs. depth. a, Radius of 59 fluorescent microspheres as functions of the Z positions (Each color corresponds to one fluorescent microsphere). **b**, Average radius of each fluorescent microsphere as functions of the average Z positions throughout the whole trajectory (Z<0 μm and Z>25 μm are removed for fitting). **c**, Average radius and Z positions of fluorescent microspheres. **d**, Two-terms exponential fit of the radius R vs. Z positions of the refined 41 fluorescent microspheres. **e**, Calibrated radius of 59 microspheres as functions of time. **f**, Histogram of the growth rates of 59 microspheres.

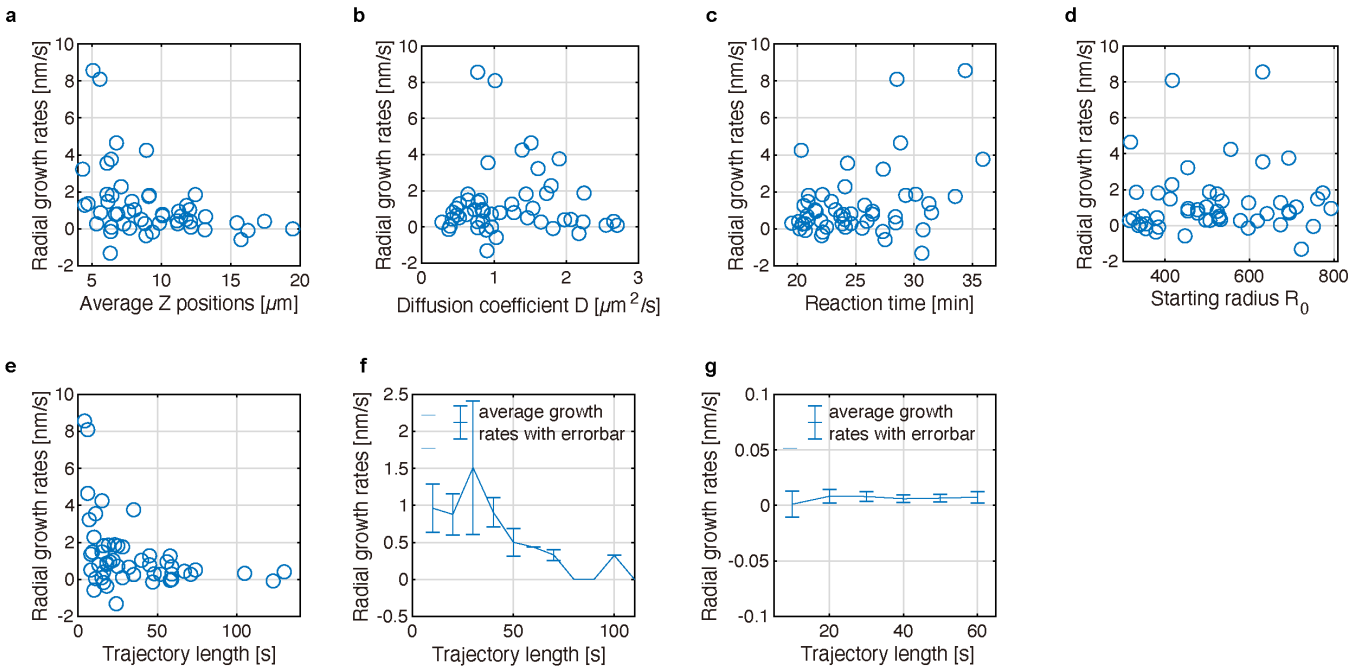

Extended Data Fig. 7 Correlation of radial growth rates with different parameters. a, Scatter plot pf radial growth rates vs. average Z position of polynorbornene particles. **b**, Scatter plot of radial growth rates vs. diffusion coefficient of polynorbornene particles. **c**, Scatter plot of radial growth rates vs. reaction time when tracking start. **d**, Scatter plot of radial growth rates vs. polynorbornene particle sizes at the beginning. **e**, Scatter plot of radial growth rates vs. trajectory length (**F**) Average growths rate of polynorbornene particles vs. trajectory length. **g**, Average growths rate of fluorescent microspheres vs. trajectory length.

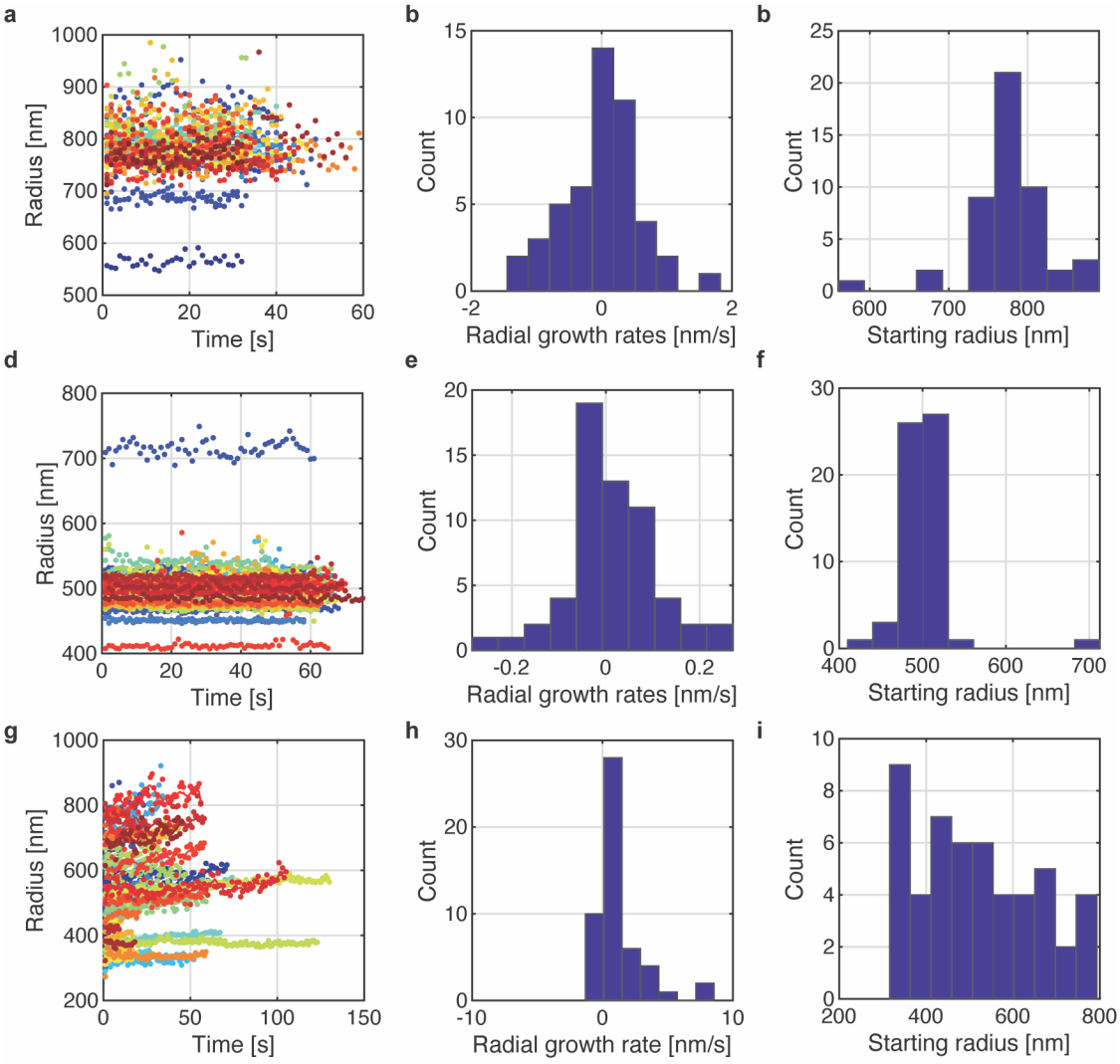

Extended Data Fig. 8 Uniform fluorescent beads vs. growing polymer particles. a, Radius of Polystyrene microspheres (dragon green, mean radius: 478 nm) as functions of time. **b**, Histogram of the growth rate of Polystyrene microspheres. **c**, Histogram of starting radius Polystyrene microspheres. **d**, Radius of Fluoresbrite carboxylate YG 1.5-micron microspheres (mean radius: 785 nm) as functions of time. **e**, Histogram of the growth rate of Fluoresbrite carboxylate YG 1.5-micron microspheres. **f**, Histogram of starting radius of Fluoresbrite carboxylate YG 1.5-micron microspheres. **g**, Radius of polynorbornene particles as functions of time. **h**, Histogram of the growth rate of polynorbornene particles. **i**, Histogram of starting radius of polynorbornene particles.

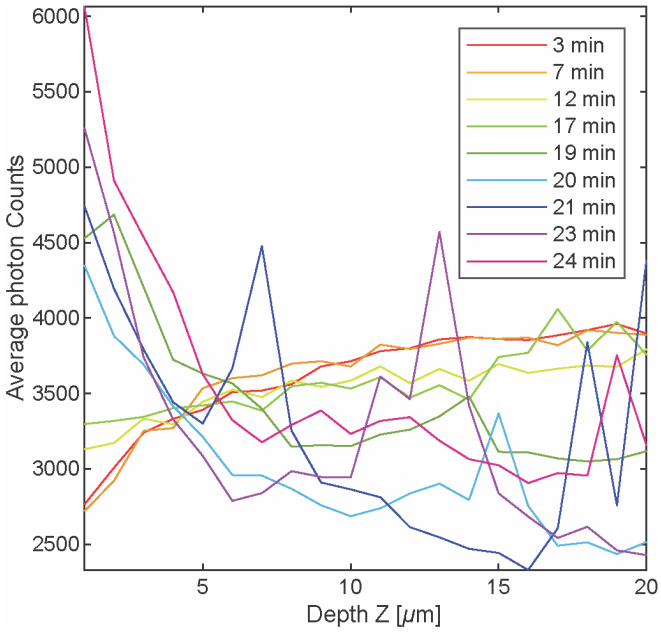

Extended Data Fig. 9 Background fluorescence intensity of solution.

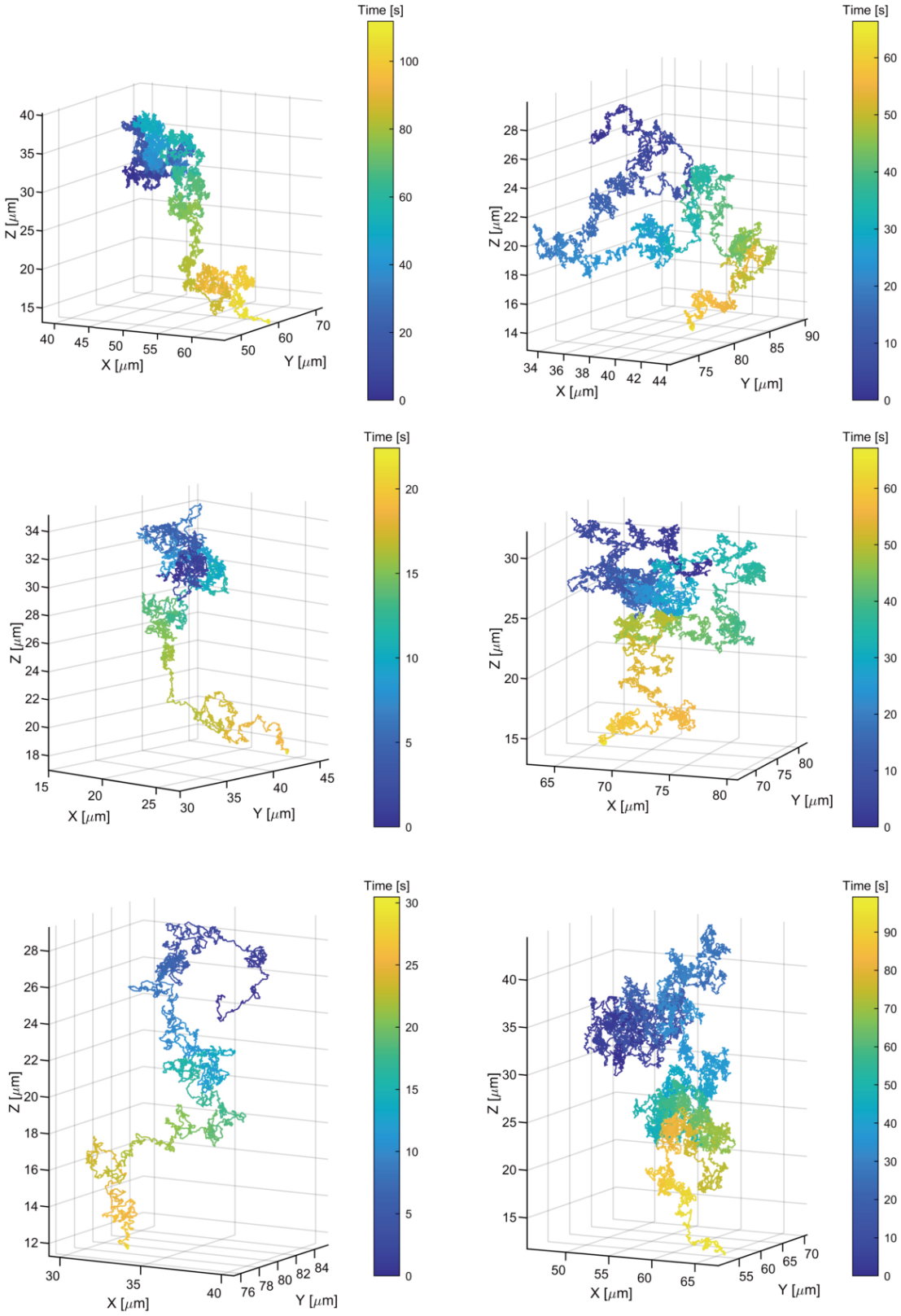

Extended Data Fig. 10 Example 3D trajectories of growing polynorbornene particles.